



Effective estimation of background light in underwater image dehazing

MIAO YANG,^{1,2,*} Bo YIN,³ ZHIQIANG WEI,^{2,3} YIXIANG DU,^{1,4} AND JINTONG Hu¹

¹School of Electronic Engineering, HuaiHai Institute of Technology, Lianyungang, Jiangsu, 222005, China

²National Laboratory of Marine Science and Technology in Qingdao, Qingdao, Shandong, 266100, China

³School of Information Engineering, Ocean University of China, Qingdao, Shandong, 266100, China

⁴School of Information and Control Engineering, Mining and Technology University of China, Xuzhou, Jiangsu, 221116, China

*lemonmiao@gmail.com

Abstract: Background estimation is a crucial step in underwater image dehazing. Most of the current estimation methods assume a uniform background light in the underwater environment and select the brightest pixel in the dark channel as the candidate, which fails to explain the real interactions of light rays and particles in the water medium and causes over-saturation in dehazed images. In this paper, the relationship between the maxima of dark channel and the background light in offshore underwater images is initially illustrated, and a contradiction of the assumption related to the dark channel prior used in underwater image restoration is addressed. To the best of our knowledge, this is the first work studying the statistical facts of underwater background light. Furthermore, a machine learning based background light estimation and reconstruction method is proposed based on the learning of the maximum areas of a dark channel. The subjective and objective restoration results of the state-of-the-art algorithms with and without applying the proposed background light estimation method to the offshore images are compared. The results show that the proposed method better simulated the directional distribution of the background light in a turbid water environment, and the foggy ambiguity caused by the backscattering was removed more efficiently in comparison with existing methods.

© 2019 Optical Society of America under the terms of the [OSA Open Access Publishing Agreement](#)

1. Introduction

The optical imaging configurations commonly used in the underwater field include cameras as well as devices such as a range-gated and synchronous scanning laser, coherent modulation and demodulation devices, structured light devices, polarization-based light devices, and non-uniform light field underwater imaging devices [1,2]. Although these devices have improved the range and clarity of the underwater imaging, every imaging system has limitations or operational requirements, *e.g.*, bulky load, low incidence power to the observation plane, large blind zone, narrow field of view, limited depth of operation, and complex operation process. At present, vision as a scientific exploration measure is becoming more and more indispensable in a marine survey. The absorption and scattering dominated by the inherent optical properties (IOPs) of the water disturb underwater imaging [3] and cause degradations when the light is traveling through the water. Namely, the forward scattering leads to blurring, and the backscattering generally reduces the image contrast, which results in an image covered by a foggy veil. Light attenuation causes the color disappeared gradually. Besides, the concentrations of the plankton, color dissolved organic matter (cDom), and total suspended matter (TSM), and distance of a target to the camera also influence the quality of underwater images [4]. Artificial lights can be used to extend the visual range, which often results in inhomogeneous lighting that manifests a bright spot in the image center surrounded by a dark area; even worse, the artificial lighting makes the scattering caused by the suspended particles aggravate. Moreover, waves, swirls, and silt also

produce irregular blurring in underwater images. Therefore, the restoration or enhancement of the underwater images is necessary.

The enhancement of underwater images has been studied in several aspects such as the image contrast [5, 6], clarity [7–9] and color compensation [10–16]. For a single image, Iqbal *et al.* [11] proposed the integrated color model (ICM) and the unsupervised color-correction method (UCM) [17]. Fu *et al.* [18] built a variational retinex model to enhance the illumination of underwater images. Chiang and Chen [19] restored the underwater images by combining the dark channel prior (DCP) based dehazing with the wavelength compensation. Ancuti *et al.* [20] enhanced the visual quality of underwater images using the fusion principles; further, they proposed an improved white balance by compensating the loss of red channel before resorting to the conventional Gray-World method [21]. The Gamma correction and a high-pass filter were adopted in the fusing process to get the final output. Since deep learning has shown remarkable performance in high-level attribute representation by constructing multi-hidden layer model and massive training data, some techniques [22,23] were used to rectify the colour distortion in underwater images. Li *et al.* [23] proposed a weak supervised color transfer method based on CycleGAN [24] to correct the color distortion of underwater images, which learns a cross domain mapping function between underwater images and air images. For the generators of forward and backward networks, the adversarial loss, cycle consistency loss and structural similarity index measure (SSIM) loss functions are included. Besides the complexity of the calculations, the clarity of input image are unrestored.

He *et al.* [25] put forward the DCP and pointed out that pixels of at least one of the three color channels in the fog-free natural images have low values, and the increased grayscales of pixels in the dark channel of a hazy image can be attributed to the haze. The background light estimation is a crucial step in the DCP based image dehazing. Fog can be removed by subtracting the background light from the degraded image. In recent years, the underwater image restoration based on the DCP has received extensive attention [26–31]. Galdran *et al.* [26] proposed the red channel prior method and estimated the background light from the pixel with the highest intensity in the red channel. Carlevaris-Bianco *et al.* [27] computed the dark channel image by the difference between the maximal value in the red channel and the maximal value in the green-blue channel, and the background light was estimated as the highest intensity of the dark channel. Peng *et al.* [28] proposed a transmission estimation by using the information on image blurriness, selected a single background light from the blurry regions in the underwater images [29], and proposed a transmission map estimation by applying the illumination differential with a known background light [30]. Li *et al.* [31] used the quad-tree subdivision and graph-based segmentation to obtain a single value of the global background light and estimated the medium transmission map by the minimum information loss principle. The mentioned DCP based methods generalized the background light conception in the air directly to the water media, while the background light in the underwater image should be related to the backscattering. In addition, these dehazing methods take the brightest pixel in dark channel as a background light, which can result in an erroneous estimation when a scene contains white or bright targets.

The backscattering light in the water manifests a non-uniform characteristic due to the complicated light-particle interactions. The concentration and composition of suspended particles in the water with a different type, current and depth, and in different season and weather conditions, make the distortions in underwater images to manifest characteristics of localization. Besides, the background light exhibits directionality characteristic for different imaging angle. A non-uniform background light has been considered by several underwater dehazing methods [20,32], but all these methods consider the maxima of the dark channel as a background light.

In this paper, the theoretical analysis of the distribution and the scale selection of background light in the underwater images are provided. The contributions of this work are as follows: (i) a new standpoint, which explains that assuming the 0.1% maxima of the dark channel as a

background light (as it is commonly used in the dehazing methods) does not correspond to the real background light in underwater image, is introduced; (ii) according to the statistical analysis of the sub-image in the collected underwater images, the local scale in the underwater background is mainly below 20% of the image size, and concentrate around 5%; (iii) a machine learning based background light estimation (MLBE) and reconstruction method is proposed based on artificial neural network (ANN), and it is applied to predict whether the maximum region of the dark channel belongs to the background area of the underwater image or not. The estimation accuracy of the background light of 91.0703% is achieved. Also, by using the proposed MLBE during the background light estimation process, the DCP based underwater image restoration can be improved in the dark area, sharpness and color restorations.

The rest of the paper is organized as follows. The underwater imaging model and related theory are presented in Section 2. In Section 3, the statistical analysis of underwater background light is introduced, and the contradiction of the traditional background light estimation methods in the DCP based underwater image restoration is pointed out. In Section 4, the framework of the proposed machine learning based background light estimation (MLBE) is described and the transmission map estimation is summarized. The experimental and comparative results are provided and discussed in Section 5. Lastly, the conclusions are given in Section 6.

2. Underwater imaging optical model

2.1. Jaffe-McGlamery model

According to the Jaffe-McGlamery underwater imaging model [33], the total radiance of an image that reaches an observer consists of three additive components: direct component E_d , forward-scattering component E_f , and backscattering component E_b , as shown in Fig. 1.

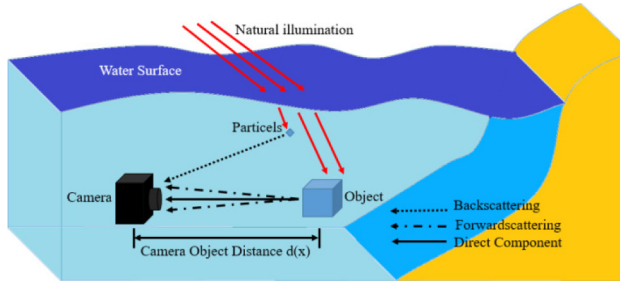


Fig. 1. The underwater imaging model.

E_d represents the attenuated version of reflected light, and is expressed as:

$$E_d = J_c(x)e^{-p_\lambda d(x)}, \quad (1)$$

where $J_c(x)$ is the radiance of the object, $c=\{R, G, B\}$ denotes the colour channel of an RGB image, $d(x)$ is the distance between the observer and object, and p_λ is the attenuation coefficient. In the underwater environment, p_λ denotes the sum of the absorption coefficient a_λ and scattering coefficient b_λ , of which both are wavelength λ dependent, which can be expressed as:

$$p_\lambda = a_\lambda + b_\lambda. \quad (2)$$

The exponential term $e^{-p_\lambda d(x)}$ is also known as the transmission map $t_c(x)$ through the water medium:

$$t_c(x) = e^{-p_\lambda d(x)}. \quad (3)$$

For offshore water (depth <20 m), E_b can be expressed as:

$$E_b(x) = B_\infty^c(x)(1 - e^{-\rho_\lambda d(x)}), \quad (4)$$

where $B_\infty^c(x)$ is known as the backscattering light of $c=\{R,G,B\}$ channel or the background light at pixel x . In general, E_f is associated with a small fraction of the overall image degradation process, and the simplified underwater optical imaging model employed in most existing dehazing techniques becomes:

$$I_c(x) = J_c(x)t_c(x) + (1 - t_c(x))B_\infty^c(x). \quad (5)$$

By inserting a raw image $I_c(x)$, $B_\infty^c(x)$ and $t_c(x)$ into Eq. (5), the restored underwater image $J_c(x)$ can be obtained from:

$$J_c(x) = \frac{I_c(x) - B_\infty^c(x)}{t_c(x)} + B_\infty^c(x). \quad (6)$$

2.2. Dark channel prior

According to the DCP [25], the dark channel L_{DC} of an underwater color image $I_c(x)$ can be derived from the minimization of a $z \times z$ local block centered at x , $\Omega(x)$ in the R , G and B channels, that is:

$$L_{DC} = \min_{y \in \Omega(x)} (\min_{c \in R,G,B} I_c(y)), \quad (7)$$

Applying the dark channel prior [25] to the original image $J_c(x)$, we have:

$$\min_{y \in \Omega(x)} (\min_{c \in R,G,B} J_c(y)) = 0. \quad (8)$$

By applying the minimum operators given by Eqs. (7) and (8) to Eq. (5), the dark channel L_{DC} of an underwater color image $I_c(x)$ becomes:

$$L_{DC} = \tilde{B}_\infty^c(x)(1 - \tilde{t}_c(x)), \quad (9)$$

where $\tilde{B}_\infty^c(x)$ and $\tilde{t}_c(x)$ are the estimated background light and transmission map respectively, as already specified.

2.3. Background light estimation

He *et al.* proposed to use the 0.1% brightest pixels of the dark channel as the global background light [25]. Although the dark channels used in the underwater image restoration or denoising have been constructed in various ways [25–31], in the majority of them the maximum of L_{DC} is still used as an estimated background lighting, *e.g.*, Li *et al.* [31] proposed a graph-based segmentation to obtain a global background light and estimated the medium transmission map by the minimum information loss principle. The score of each region was computed by the absolute difference between the regional average and standard deviation, and a flat region B_s with the highest score was extracted, and then segmented to remove the influence of the target. Finally, the pixel with the maximum blue-red difference in the 0.1% of the brightest pixels of the flat region B_s was selected as a background light pixel.

$$\tilde{B}_\infty^c(x) = I_c(\arg \max_{x \in B_s, 0.1\%} |I_R(x) - I_B(x)|). \quad (10)$$

Galdran *et al.* [26] proposed the red channel hypothesis in which the background light \tilde{B}_∞^c was estimated by choosing the brightest pixel in the red channel as follows:

$$\tilde{B}_\infty^c(x) = (I_R(x_0), I_G(x_0), I_B(x_0)) \quad I_R(x_0) \geq I_R(x) \forall x. \quad (11)$$

The method proposed by Carlevaris-Bianco *et al.* [27] estimates the transmission map $\tilde{t}_c(x)$ from the maximum difference between the blue-green and red channels and uses the minimum of the

transmission map as a background light, which is given by:

$$\tilde{B}_{\infty}^c(x) = I_c(\arg \min_x \tilde{t}_c(x)). \quad (12)$$

Peng *et al.* [28] estimated the global background light image by averaging the 0.1% brightest pixels in L_{DC} :

$$\tilde{B}_{\infty}^c(x) = \frac{1}{|S_{0.1}|} \sum_{x \in S_{0.1}} I_c(x), \quad (13)$$

where $S_{0.1}$ represents the 0.1% brightest pixels in L_{DC} . Ancuti *et al.* [20] applied the local maxima in the dark channel and estimated the background light by:

$$\tilde{B}_{\infty}^c(x) = \max_{y \in M_{DC}^{\Psi(x)}} \left(\min_{z \in \Omega(y)} I_c(z) \right), \quad (14)$$

where $M_{DC}^{\Psi(x)}$ is the pixel in $\Psi(x)$, and $\Psi(x)$ is the local window in L_{DC} centered at x , the maximum of $\Psi(x)$ is y , and z represents the pixel in $\Omega(y)$.

Whereas, the underwater images are degraded by the comprehensive light attenuation due to the IOPs of pure water, the solute in seawater (molecular scattering and absorption), and suspended particles in the water in general (particle scattering and absorption). As the imaging effects also depend on the distance of the objects, the degradations are local and cannot be corrected by global operations. The background light is generated by scattering of the ambient light from a large range of angles. The related research has shown that the light rays traveling in the underwater environment encountered the beam-particle interaction with different random times [34]. A single background light value over the entire image fails to explain the real interactions of light rays and particles in the water medium. On the other hand, since the 3-D space should be sliced into planes to calculate the backscattering irradiance of every small plane in different directions and distances relative to the camera, the background light can be regarded as a superposition of many point-sources of the light in the space, which produces a non-uniform image intensity.

3. Contradiction with classical DCP

3.1. Directionality of background light in offshore underwater images

Often, it is assumed that the background light is uniformly distributed to the target at the same distance from infinity in natural image defogging. However, not only the natural lighting from the water surface but also the artificial lighting is commonly used in underwater imaging. The background light in the underwater images shows directional characteristics due to the angles of photography and irradiance distributions of the artificial light.

In the offshore area, the concentrations of cDOM and TSM are higher than in the far-shore area because of the impact of terrigenous input and sediment resuspension [35–36]. Therefore, the light propagation incurs strong interaction with random particles, which means that the backscattering is one of the most important factors in degradation of offshore underwater images.

Considered that the current dehazing methods mainly aim to the underwater images taken under shallow water, we collected 300 daytime offshore (depth < 20 m) underwater images including the sea farming, sea creature investigation, and coastal underwater engineering, and some of them are given in Section 5. The water (body) background areas were interactively selected to constitute a collection of the offshore underwater background images. To illustrate the directionality of the background light in the offshore underwater images, the linear fitting angles of column cumulative and average brightness distributions of the background images were analyzed, as shown in Fig. 2. In Fig. 2, it can be seen that the average brightness distribution of underwater background images had obvious directionality. The fitted angles of the underwater

background light were all between -45° and 45° , which was correlated with the viewing angle and the relative position of lighting sources. Therefore, assuming a single global background light value as some of the DCP based underwater restorations was not in accordance with the actual situation.

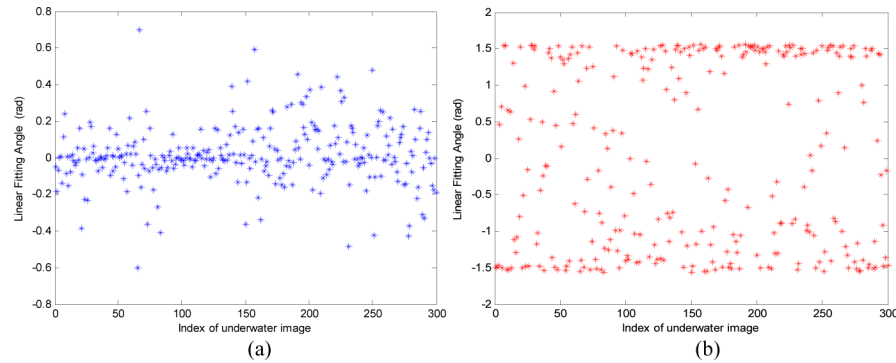


Fig. 2. Fitted directional angles of the brightness of the background image: (a) column average intensity, (b) column cumulative intensity.

3.2. Relationship between background light and dark channel for underwater images

The early dehazing methods for natural images take the brightest pixel in a scene as a background light [37,38]. However, such an approach can result in an erroneous estimation when a scene contains white or bright targets. Some hierarchical veiling light estimation methods for natural image dehazing [39–43] demonstrated the improved performance in the case of terrestrial scenes containing bright objects.

In order to illustrate the relationship between the pixel values of background light and dark channel in underwater environments, the following experiments were conducted. For 300 offshore underwater color images, the typical background pixels in each image were manually selected, and compared with the pixels in the maximum areas of the dark channel. The distribution of the ratios of dark channel maximum area belonging to the true background in 300 underwater images is shown in Fig. 3(a), and it can be seen that the extreme areas of the dark channel mostly belonged to the background lights of the underwater images. In Fig. 3(b), the histogram of the pixel values in the maximum area of the dark channel divided by the global maximum of the dark channel in 300 underwater images is presented. We noticed that the pixels in the maximum areas were not equal to the brightest value of the dark channel, as presented in Fig. 3(b); their ratios to the global maxima of the dark channel were distributed between 0 and 1, instead of the first 0.1% or 10% maxima of the dark channel images or the minima of the transmission maps, which was adopted in the classical dark channel prior theory. Since each underwater image was different in content, the proportions of pixels in the maximum areas of the dark channel to the true background were also different.

3.3. Background intensity localization

To verify the real distribution of underwater environment lighting, the intensity of ambient light obtained of different areas on a flat target surface (the checkerboard with the size of 110 cm \times 182 cm, containing 10 \times 7 patches) placed in a tank was measured as shown in Fig. 4. The tank had the length of 2 m, the width of 1.2 m, and the height of 1 m. Every test was repeated for five times under the conditions of clear, median muddy, and turbid water [44], respectively. The average illuminance of each block was computed, and the results are shown in Fig. 5. The

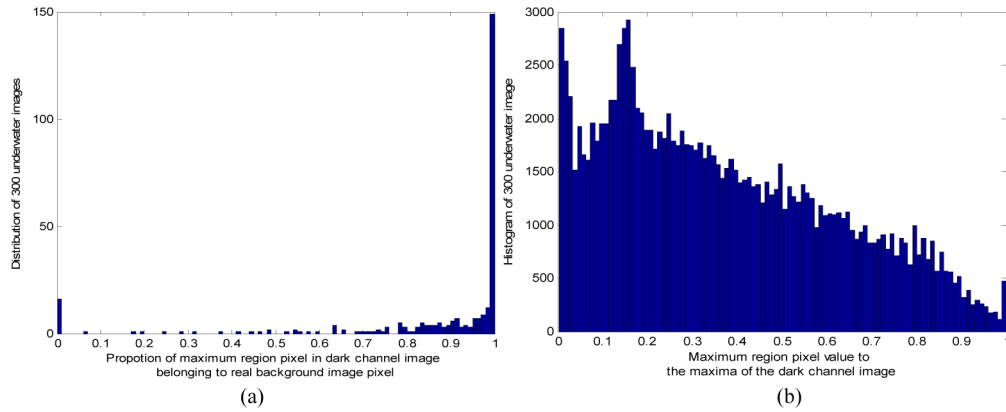


Fig. 3. The relationship between the background pixels and dark channel maximum area of the offshore underwater images. (a) The histogram of the ratios of the maximum area in the dark channel belonging to the true background light in 300 underwater images. (b) The histogram of the pixel values in the maximum area of the dark channel divided by the global maxima of the dark channel in 300 underwater images.

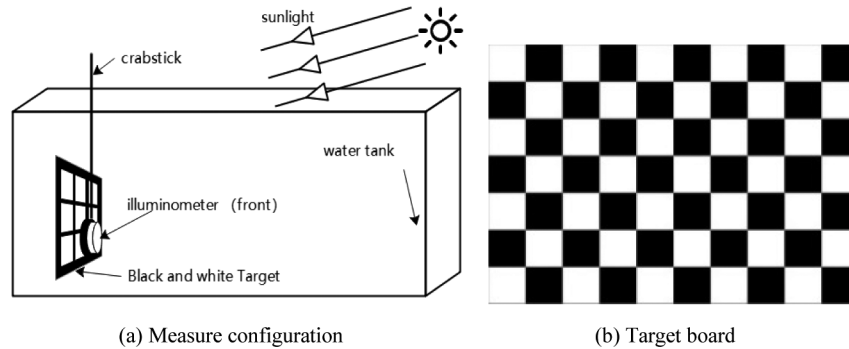


Fig. 4. Illuminance measurement.

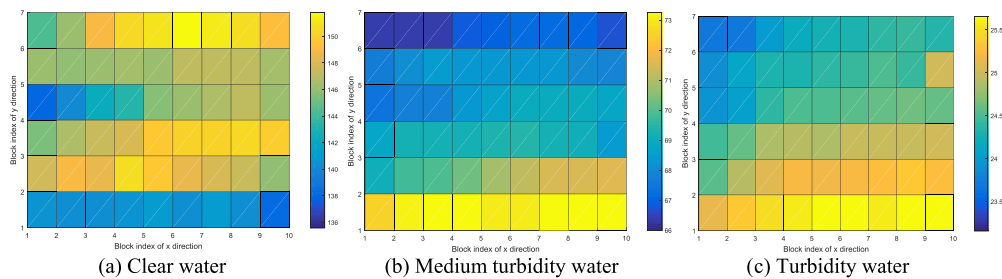


Fig. 5. Illuminance distribution of the target panel under natural lighting conditions.

centers of the target board in Figs. 5(a)-(c) were 55 cm, 53 cm, and 53 cm from the water surface, respectively. The intensity of illuminance on the water surface in Figs. 5(a)-(c) was 344-390 lx, 177-196 lx, and 63-78 lx, respectively. As Fig. 5 illustrates, the underwater lighting illuminance were not uniform along the image plane but related to the position of the light source and water body.

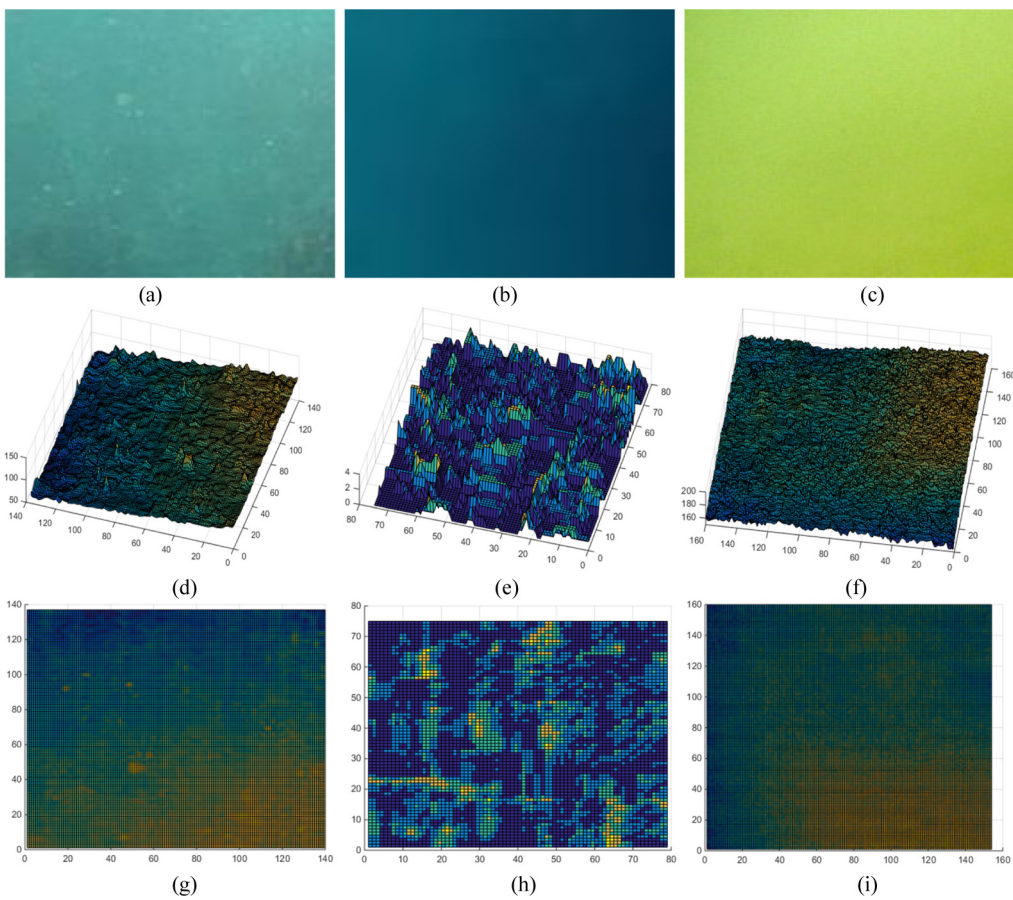


Fig. 6. The *R*-channel luminance distribution of the background areas in underwater images. (a)-(c) The original underwater background images, (d)-(f) the fitted *R*-channel luminance in the 3D view, (g)-(i) the fitted *R*-channel luminance in the plan view.

Furthermore, the brightness distribution of the background areas in real underwater images is shown in Fig. 6. In Figs. 6(a)-(c), the background patches of three underwater images are presented. The distributions of *R* component of these patches in 3D and plan views are fitted in Figs. 6(d)-(i). In addition to the non-uniformity brightness presented in Figs. 6(d)-(i), due to the sea snow, the bright light caused by particle scattering existed in the background images and exhibited the local Gaussian-like pattern, as shown in Figs. 6(d)-(f).

Therefore, by estimating the background light locally in the restoration of underwater images, the under- or over-saturation could be avoided while recovering the underwater images with better clarity. The statistics on the scale of local distribution of the middle row for 300 offshore underwater background images was also carried out, and the results are shown in Fig. 7. Based on the results presented in Fig. 7, it can be concluded that local scales of the underwater background image intensity were mainly below 20% of the image size and it was about 5%.

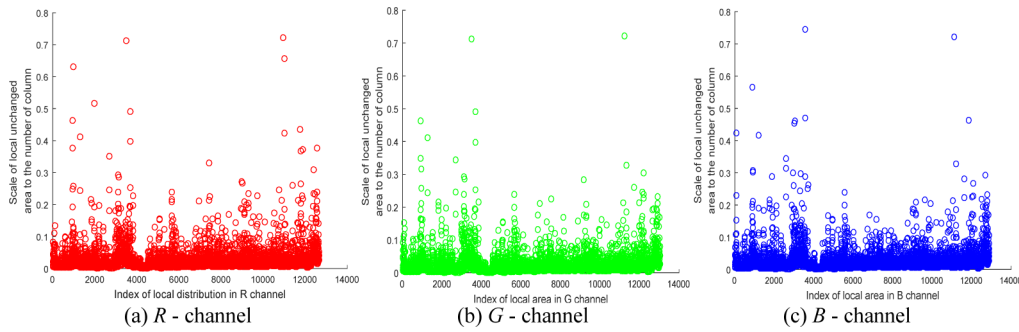


Fig. 7. Luminance distributions of the middle row in *R*, *G*, and *B* channels of the offshore underwater background images.

4. Machine learning based background light estimation

4.1. ANN based background light estimation

In this work, we propose an ANN-based model to distinguish the maximum area of the dark image channel which originates from a real water background, as shown in Fig. 8. The proposed model was trained with 300 real offshore underwater images. In order to obtain the best performance, a three-layer back propagation (BP) neural network with the tangent-sigmoid activation function in all hidden layers was used, and both input and output values were normalized on the scale of 0 to 1. The background light was estimated by the Gaussian guided morphological reconstruction based on the nearest neighbor interpolation. The training data was obtained by labeling the true background pixels in the underwater images interactively.

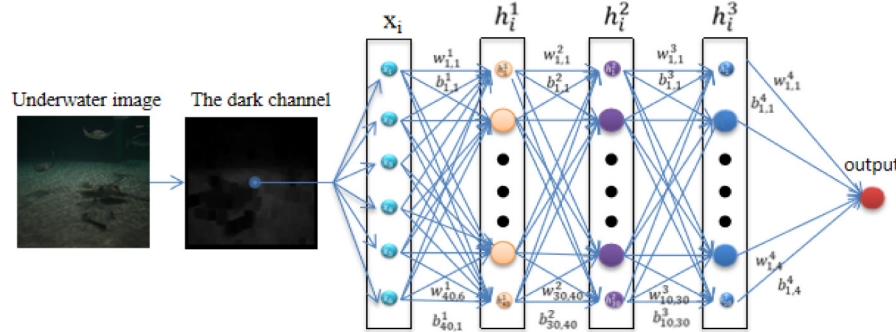


Fig. 8. The structure of the ANN model for the background light recognition.

Let M_{DCi} be the maximum area i in the dark channel image L_{DC} of an underwater image. Thus, when the pixels included in M_{DCi} were close to the true water background, the label $y(i)$ of M_{DCi} was equal to 1. As the input used in training, six different features from each maximum area M_{DCi} were extracted:

$$x_{DC}^{(i)} = \{R_{DC}^{(i)}, G_{DC}^{(i)}, B_{DC}^{(i)}, V_{RGB}^{(i)}, V_{DC}^{(i)}, L_{DC}^{(i)}\}. \quad (15)$$

In Eq. (15), $R_{DC}^{(i)}$, $G_{DC}^{(i)}$, $B_{DC}^{(i)}$, $V_{RGB}^{(i)}$ denote the normalized color means and the standard color deviation of pixels in M_{DCi} , $V_{DC}^{(i)}$ is the standard deviation of M_{DCi} , and $L_{DC}^{(i)}$ is the normalized pixel value in M_{DCi} .

The background light pixels were obtained from the nearest interpolation. The proposed machine learning based background light estimation (MLBE) for an underwater image $I_c(x)$ can

be defined as:

$$\left\{ \begin{array}{ll} \tilde{B}_{\infty}^c(x) = I_c(x), & x \in M_{DC}^{y^{(i)}=1} \\ \tilde{B}_{\infty}^c(x) = \text{Mean}_{z \in M_{DC}^{y^{(i)}=1}}(I_c(z)), & \text{otherwise} \end{array} \right. , \quad (16)$$

where $M_{DC}^{y^{(i)}=1}$ denotes the maximum area i of the dark channel with the label value of $y^{(i)} = 1$, $i = 1, 2, \dots, n$, where n is the total number of maximum areas of the dark channel with the label of 1; $N_{M_{DC}^{y^{(i)}=1}}^i$ denotes the pixels surrounding $M_{DC}^{y^{(i)}=1}$. The Gaussian filtered R , G , and B images with a scale of 2% of the image size were applied as the guided image to reconstruct the interpolated background light image. An example of the proposed MLBE is shown in Fig. 9. The outputs of the other background light estimations are shown in Figs. 9(b)-(e). For the mist-like underwater images shown in Fig. 9(a), the MLBE achieved the background light images having the object scattering light distribution which was more similar to the real one than those obtained by the other methods were.

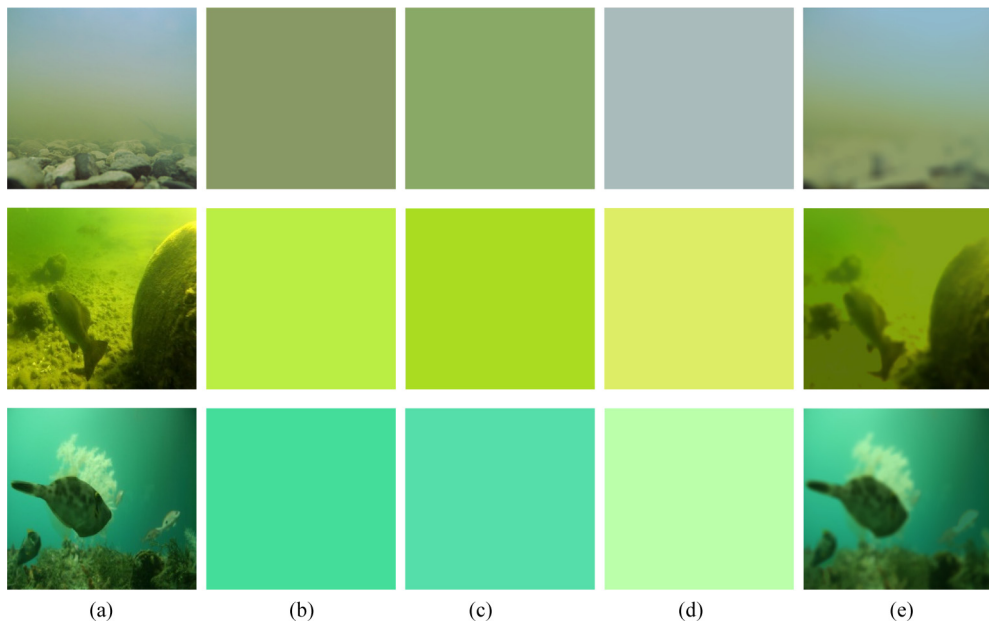


Fig. 9. Examples of the background light estimation. (a) The original images, (b) the images obtained by the method proposed by Galdran *et al.* [26], (c) the images obtained by the method proposed by Peng *et al.* [28], (d) the images obtained by the method proposed by Li *et al.* [31] and (e) the images obtained by using our MLBE method.

4.2. Transmission map estimation

Assuming the background light was known, Ancuti *et al.* [20] used the DCP to estimate the transmission map by:

$$\tilde{t}_c(x) = 1 - \min_{y \in \Omega(x)} \left(\min_{c \in \{R, G, B\}} \frac{I_c(y)}{\tilde{B}_{\infty}^c(y)} \right). \quad (17)$$

Carlevaris-Bianco *et al.* [27] calculated the dark channel using the difference $D(x)$ between the maximum in the red channel and the other channels (green and blue):

$$D(x) = \max_{x \in \Omega, c \in R} I_c(x) - \max_{x \in \Omega, c \in \{G, B\}} I_c(x). \quad (18)$$

The transmission map was estimated by adjusting the difference until it became equal to 1, which is given by:

$$\tilde{t}_c(x) = D(x) + (1 - \max_x D(x)). \quad (19)$$

The red channel prior proposed by Galdran *et al.* [26] exploited the reciprocal of global background light and minimization on the R , G and B channel to obtain the transmission map of the red channel:

$$\tilde{t}_c(x) = 1 - \min \left(\frac{\min_{y \in \Omega(x)} (1 - I_R(y))}{1 - \tilde{B}_{\infty}^R}, \frac{\min_{y \in \Omega(x)} I_G(y)}{\tilde{B}_{\infty}^G}, \frac{\min_{y \in \Omega(x)} I_B(y)}{\tilde{B}_{\infty}^B} \right). \quad (20)$$

Let $I(x)$ be the grayscale version of $I_c(x)$ and $G^{k,\sigma}$ be the input image filtered by $k \times k$ Gaussian filter with the variance σ^2 ; Peng *et al.* [28] proposed a fuzzy map $B(x)$ which is given by:

$$B(x) = \frac{1}{n} \sum_{i=1}^n (|I(x) - G^{r_i, r_i}(x)|). \quad (21)$$

In Eq. (21), $r_i = 2^i n + 1$, and $n = 4$. The transmission map was estimated by using the local maximum of the fuzzy map:

$$\tilde{t}_c(x) = \max_{y \in \Omega(x)} B(y). \quad (22)$$

Given the global background light of the red channel \tilde{B}_{∞}^R , Li *et al.* [31] estimated the transmission map of the red channel utilizing the principle of minimum information loss:

$$\tilde{t}_R(x) \geq \max \left[\min_{y \in \Omega(x)} \left(\frac{I_R(y) - \tilde{B}_{\infty}^R}{-\tilde{B}_{\infty}^R} \right), \max_{y \in B_s} \left(\frac{I_R(y) - \tilde{B}_{\infty}^R}{255 - \tilde{B}_{\infty}^R} \right) \right]. \quad (23)$$

Then, the transmission map of G and B channels was obtained by using the attenuation coefficient priors:

$$\tilde{t}_c(x) = (t^R(x))^{p^c/p^R}, \quad c \in \{G, B\}, \quad (24)$$

$$\frac{p^c}{p^R} = \frac{b^c \tilde{B}_{\infty}^R}{b^R \tilde{B}_{\infty}^c}, \quad (25)$$

$$b^c = (-0.00113 \lambda_c + 1.62517) b(555\text{nm}). \quad (26)$$

Generally, in the water, λ_R , λ_G , and λ_B are respectively 620 nm, 540 nm, and 450 nm, and $b(555\text{nm})$ is the scattering coefficient at a particular wavelength of light [45]. However, when the theoretical maximum of a background light was used as a denominator in the computing of transmission map, the over saturation would cause the artifacts in the background area due to low transmission values.

5. Experiments and discussion

The proposed approach was validated on hundreds of underwater images. The data included 300 images collected online which associated with the offshore investigation and sea farming and had the size from 194×259 to 3968×2976 pixels. Matlab ANN fitting tool was used to study the features and the corresponding labels of the maximum areas of the dark channel. The

three-layer BP neural network was adopted to the classification of 131,544 maximum areas of the dark channels for 300 underwater images. The proportion of the data samples used in training, verification, and test was 70%, 15%, and 15%, respectively. The transfer functions of hidden layers were all the tangent-sigmoid function, and linear function (pureline) was used as the activation function of the output layer. The model achieved the accuracy of 91.0703% on test data.

The restoration methods were evaluated by comparing the obtained improvements when the MLBE was used. In the experiments, the block size of the dark channel and Gaussian filter was 15×15. Some of these experimental results are shown in Fig. 10. The existing techniques including that proposed by Peng *et al.* [28] and Li *et al.* [31]. It can be seen from the results that the tested methods produced better sharpness and color restoration effects by applying the proposed MLBE during the background light estimation process (the transmission map estimation remains unchanged), as shown in Fig. 10. From the visual analysis, some areas in the results recovered by [28] suffered from under-saturation, as shown in the first three pictures in Fig. 10(b). By using the MLBE, more uniform contrasts were boosted than when the original method of Peng *et al.* [28] was used, as shown in Fig. 10(c). As shown in Fig. 10(d), the method proposed by Li *et al.* [31] recovered the color casting of the underwater images but had blurred details; but, combining this method with the proposed MLBE the dark area was improved and clear detail of the objects in the testing images was obtained.

Two underwater images with bright targets or corrugated light existed and the restoration results of them with or without applying MLBE are given in Fig. 11. The existing dehazing methods, such as methods proposed by Peng *et al.* [28] and Li *et al.* [31], usually take the brightest pixel in the dark channel as a background light, which result in over saturation in the corner of the restored image but flare patches at the reflect light spots on the metals as shown in the second pictures of Figs. 11(a)-(b). For the corrugated light commonly visible in shallow underwater image, single background image pixel caused fake contours since the background lights supposed to be uniform in the fifth images of Figs. 11(a)-(b). However, by using the proposed MLBE in the restoration, not only the veiling effects covered the original images were relieved, but also the global contrast was improved, as shown in the pictures in the last column of Figs. 11(a)-(b).

The Chroma variance, contrast of brightness, and saturation of the underwater color images were proved to concur well with the observers' perceptions [46]. These indexes, constituted an underwater color image quality evaluation (UCIQE) [46], which has been widely used to evaluate the quality of underwater color images [29,31,47]. The quantitative measurements of the images which are shown in Fig. 10 are listed in Table 1. As Table 1 shows, the UCIQE values were improved when the proposed MLBE method was applied to the background light estimation for underwater images restorations. For the second images in Fig. 10(a), the image restored by the method of Peng *et al.* [28] with the MLBE is shown in Fig. 10(c), and it can be seen that the highest UCIQE values was achieved. For the third picture in Fig. 10(a), the high-lighting areas in the restored images produced by the original method of Peng *et al.* [28] (shown in the third picture in Fig. 10(b)) resulted in the higher chroma variance and further influenced the final UCIQE values, as shown in Table 1. It can also be seen in Table 1 that the results when the proposed MLBE and the transmission map estimation based on the minimum information loss of Li *et al.* [31] were adopted the higher contrast gains and the best synthetic objective and subjective performances for the first and fourth images in Fig. 10(a) were achieved.

Imatest [48] has been the most professional software for qualifying the camera imaging by comparing the difference between the real images of charts and the testing ones. To further verify the restoration capability of the proposed MLBE regarding the contrast, clarify and colourfulness objectively, the restoration effects were compared with the real color images and analyzed by presenting the quality of the restored Imatest 4.3 SFR board and ColorChecker 24 X-Rite Chart



(a) Original images.

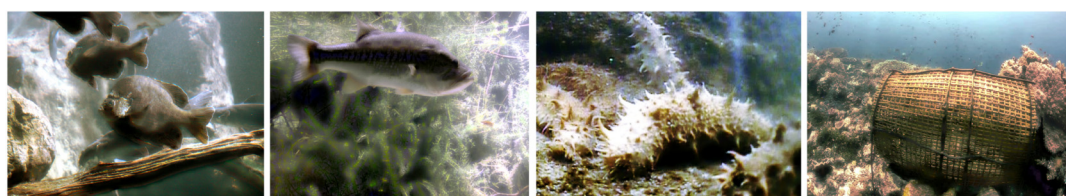
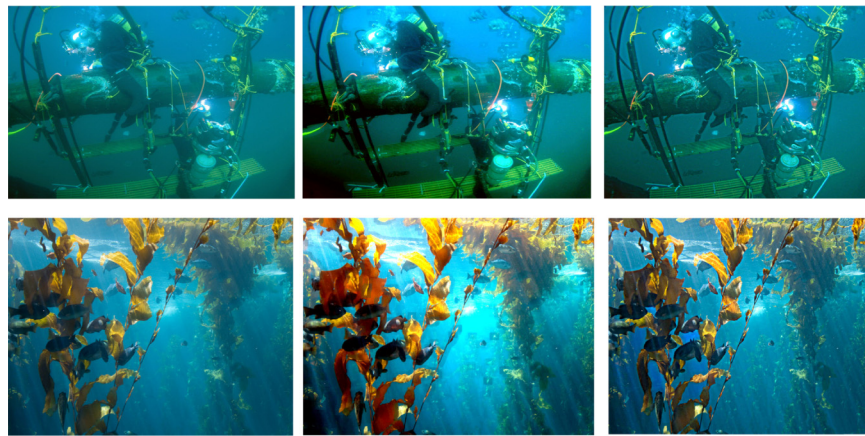
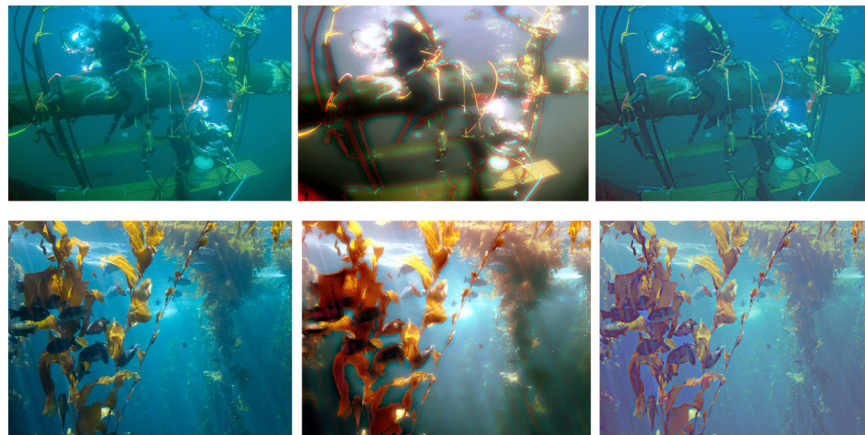
(b) The outputs of Peng *et al.* [28].(c) The results of Peng *et al.* [28] with MLBE used.(d) The outputs of Li *et al.* [31].(e) The results of Li *et al.* [31] with MLBE used.

Fig. 10. Comparisons of underwater image restoration results, from the up to the down are: original images, results of cited methods and improved results with MLBE used.

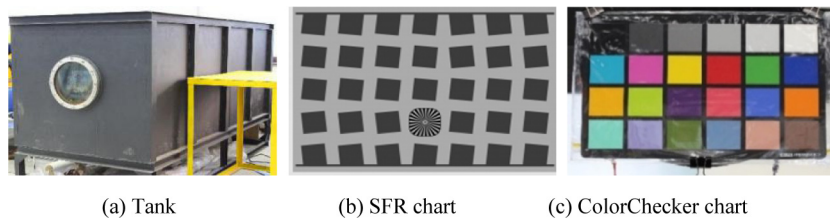
(a) Comparisons of underwater image restoration results of Peng *et al.* [28](b) Comparisons of underwater image restoration results of Li *et al.* [31]**Fig. 11.** Comparisons of underwater image restoration results, from the left to the right are: original images, results of cited methods and improved results with MLBE used.

(21.59×27.94 cm) taken in a tank. The tank was 2.53 m long, 1.02 m wide, and 1.03 m high, as shown in Fig. 12. The chart images were taken with OTI-UWC-325/P/E color camera. The images (with the size of 960×576) were obtained in the water with the transparency of 325 cm [44] under natural lighting at the distance of 70 cm and 110 cm from the camera with the LED lighting, respectively. The restored images are illustrated in Figs. 13 and 14.

The relative contrast at a given spatial frequency (output contrast/input contrast) is called the modulation transfer function (MTF). The spatial frequencies where MTF is 50% of its low frequency value (MTF50) are empirically used as the best indicators of image sharpness, and the ratio of unit line width to the picture height (LW/PH) is commonly adopted for digital sensors [48]. The output data of Imatest 4.3 is given in Table 2. The data show that when the MLBE was used, the methods achieved better clarity. The capabilities of color restoration when the MLBE was applied were indicated by the color error in the device-independent CIELAB color space. The CIELAB was designed to be perceptually uniform, meaning that the perceived difference between the colors was approximately proportional to the Euclidean distance between them; ΔE^*_{ab} (included luminance L^*) and ΔC_{ab}^* (included only the color, omitting L^*), which are

Table 1. Quantitative Measurement Results

Algorithm	Raw image	Peng <i>et al.</i> [28]		Li <i>et al.</i> [31]	
		Original	MLBE	Original	MLBE
Contrast	0.6863	0.9843	0.8235	0.9922	0.9882
	0.8275	0.8196	0.9333	0.8275	0.9882
	0.7176	0.9725	0.7804	0.9922	0.9922
	0.8118	0.9843	0.9176	0.9804	0.9882
Average saturation	0.8484	0.8161	0.8485	0.8310	0.8300
	0.8369	0.7516	0.8385	0.8369	0.8322
	0.7904	0.8092	0.7909	0.8313	0.8309
	0.7681	0.8387	0.7692	0.8298	0.8293
Variance of chroma	0.3201	0.3806	0.3472	0.2888	0.3164
	0.2842	0.3145	0.3130	0.2842	0.2407
	0.3287	0.3764	0.3325	0.3315	0.3161
	0.4237	0.5164	0.4256	0.3704	0.3879
UCIQE	0.5567	0.6585	0.6071	0.6216	0.6332
	0.5757	0.5658	0.6187	0.5757	0.5983
	0.5544	0.6516	0.5735	0.6416	0.6343
	0.6190	0.7279	0.6492	0.6562	0.6665

**Fig. 12.** Tank and targets.

listed in Table 3, were computed by:

$$\Delta E^*_{ab} = ((L_2^* - L_1^*)^2 + (a_2^* - a_1^*)^2 + (b_2^* - b_1^*)^2)^{1/2}, \quad (27)$$

$$\Delta C_{ab}^* = ((a_2^* - a_1^*)^2 + (b_2^* - b_1^*)^2)^{1/2}, \quad (28)$$

where ΔC_{ab}^* or ΔE^*_{ab} of about 1 corresponded roughly to the just noticeable difference (JND) between colors. All measures showed that when the MLBE was utilized in the DCP based underwater restoration, lower ΔC_{ab}^* and ΔE^*_{ab} , and higher MTF values were achieved compared with the referred original methods.

Table 2. Imatest 4.3 SFR Analysis

SFR/analysis	MTF50 /(LW/PH) original	MTF50 /(LW/PH) with MLBE
Ancuti <i>et al.</i> [20]	13.14	22.49
Peng <i>et al.</i> [28]	14.34	48.31
Li <i>et al.</i> [31]	62.8	87.22

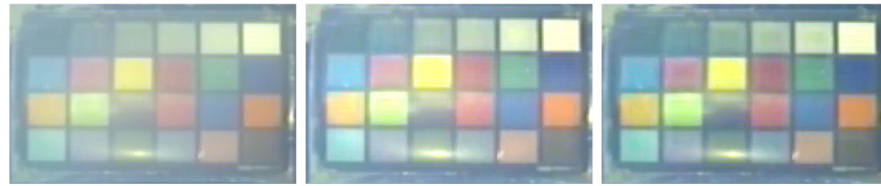
(a) The method proposed by Ancuti *et al.* [20].(b) The method proposed by Peng *et al.* [28].(c) The method proposed by Li *et al.* [31].

Fig. 13. Comparisons of underwater ColorChecker chart restorations results, from the left to the right are: original images, results of original methods and improved results with MLBE used.

Table 3. Imatest 4.3 ColorChecker Analysis

Colour/analysis	$\Delta E^*_{ab} / \Delta C_{ab}^*$ original	$\Delta E^*_{ab} / \Delta C_{ab}^*$ with MLBE
Ancuti <i>et al.</i> [20]	36/24.6	30.8/24.2
Peng <i>et al.</i> [28]	58.8/43.8	29.1/23.2
Li <i>et al.</i> [31]	52.5/41.2	52.4/40.8

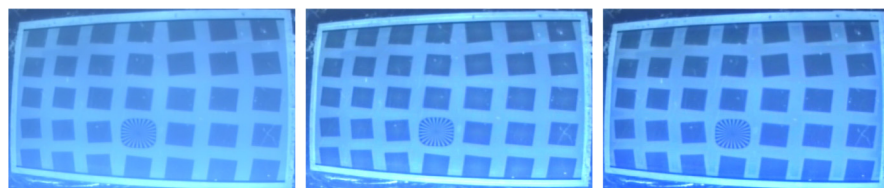
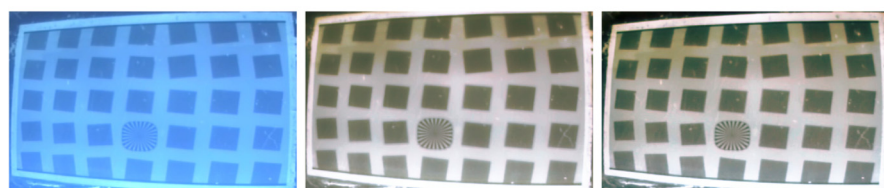
(a) The method proposed by Ancuti *et al.* [20].(b) The method proposed by Peng *et al.* [28].(c) The method proposed by Li *et al.* [31].

Fig. 14. Comparisons of underwater Imatest SFRplus restorations results, from the left to the right are: original images, results of original methods and improved results with MLBE used.

6. Conclusion

By analyzing the background patches in the underwater image set, a contradiction of the background light estimation in underwater image restoration based on the dark channel prior is found. The scale and directivity of the background light are analyzed in detail. A background light estimation method that applies the ANN to the maximum areas of the dark channel is proposed. The unphysical saturation and blurring caused by using the maximum of the dark channel as the global background light are avoided. The experiments were conducted on the tank and near-shore underwater images using different background light estimation methods, and the results proved that when the proposed MLBE was used, the distribution of light in turbid environments was more realistic and the blurring was removed more efficiently.

Funding

National Natural Science Foundation of China (NSFC) (61601194); “Six talent peaks” project in Jiangsu Province (No. DZXX-030); Lianyungang “521” funded project; Lianyungang “Haiyan” funded project.

References

1. J. S. Jaffe, “Underwater optical imaging: The past, the present, and the prospects,” *IEEE J. Oceanic Eng.* **40**(3), 683–700 (2015).
2. B. Zheng, H. Zhang, H. Zheng, and T. A. Gulliver, “Underwater Imaging Based on Inhomogeneous Illumination,” *2011 IEEE Pacific Rim Conference on Communications, Computers and Signal Processing (PacRim)*, 873–876 (2011).
3. G. Johnsen, Z. Volent, E. Sakshaug, F. Sigernes, and L. H. Pettersson, “Remote sensing in the Barents Sea,” in *Ecosystem Barents sea*, E. Sakshaug, G. Johnsen, and K. Kovacs, (eds.), (Tapir Academic Press, 2009), pp. 139–166.
4. K. Ingrid, “Underwater Imaging and the effect of inherent optical properties on image quality,” Norwegian University of Science and Technology, Master thesis (2014).
5. R. Rai, P. Gour, and B. Singh, “Underwater Image Segmentation using CLAHE Enhancement and Thresholding,” *Int. J. Emerg. Technol. Adv. Eng.* **2**(1), 118–123 (2012).
6. D. Jia and Y. Ge, “Underwater Image De-Noising Algorithm Based On Nonsubsampled Contourlet Transform And Total Variation,” *2012 International Conference on Computer Science and Information Processing (CSIP)*, 76–80 (2012).
7. A. Arnold-Bos, J. P. Malkasse, and G. Kerven, “A preprocessing framework for automatic underwater images denoising,” in *Proceedings of the European Conference on Propagation and Systems*, Brest, France (2005).
8. Y. Nie and Z. Y. He, “Underwater imaging and real-time optical image processing under illumination by light sources with different wavelengths,” *Acta Opt. Sin.* **34**(7), 0710002 (2014).
9. S. Bazeille, I. Quidu, L. Jaulin, and J. P. Malkasse, “Automatic underwater image pre-processing,” in *Proceedings of the Characterizations du Milieu Marin (CMM '06)*, 16–19 (2006).
10. M. Chambah, D. Semani, A. Renouf, P. Courtellemont, and A. Rizzi, “Underwater color constancy: enhancement of automatic live fish recognition,” in *Color Imaging IX: Processing, Hardcopy, and Applications, Proceedings of SPIE*, 5293, 157–168 (2003).
11. K. Iqbal, R. Abdul Salam, A. Osman, and A. Zawawi Talib, “Underwater image enhancement using an integrated colour model,” *Int. J. Comp. Sci.* **34**, 2 (2007).
12. G. Dudek, “Color correction of underwater images for aquatic robot inspection,” *International Workshop on Energy Minimization Methods in Computer Vision and Pattern Recognition Springer*, Berlin, Heidelberg, 60–73 (2005).
13. J. Åhlén, D. Sundgren, and E. Bengtsson, “Application of underwater hyper spectral data for color correction purposes,” *Pattern Recognit. Image Anal.* **17**(1), 170–173 (2007).
14. F. Petit, A.-S. Capelle-Laize, and P. Carré, “Underwater image enhancement by attenuation inversion with quaternions,” in *Proceedings of the IEEE International Conference on Acoustics, Speech and Signal Processing (ICASSP '09)*, 1177–1180, (2009).
15. A. T. Çelebi and S. Ertürk, “Visual enhancement of underwater images using Empirical Mode Decomposition,” *Expert Syst. Appl.* **39**(1), 800–805 (2012).
16. C. O. Ancuti, C. Ancuti, T. Haber, and P. Bekaert, “Enhancing underwater image and videos by fusion,” In *Proc. CVPR*, 81–88 (2012).
17. K. Iqbal, M. Odetayo, A. James, and R. Abdul Salam, “Enhancing the low quality images using unsupervised colour correction method,” in *IEEE International Conference on Systems Man and Cybernetics (SMC)* (2010).
18. X. Fu, P. Zhuang, and Y. Huang, *et al.*, “A retinex-based enhancing approach for single underwater image, “ *Image Processing (ICIP), 2014 IEEE International Conference on*, IEEE, 4572–4576 (2014).

19. J. Y. Chiang and Y. C. Chen, "Underwater image enhancement by wavelength compensation and dehazing," *IEEE Trans. Image Process.* **21**(4), 1756–1769 (2012).
20. C. Ancuti, C. O. Ancuti, T. Haber, and P. Bekaert, "Enhancing underwater images and videos by fusion," in *Processing of IEEE Conference on Computer Vision and Pattern Recognition*, 81–88 (2012).
21. C. O. Ancuti, C. Ancuti, C. DeVleeschouwer, and P. Bekaert, "Color balance and fusion for underwater image enhancement," *IEEE Trans. Image Process.* **27**(1), 379–393 (2018).
22. J. Li, K. A. Skinner, and R. M. Eustice, *et al.*, "WaterGAN: Unsupervised generative network to enable real-time color correction of monocular underwater images," *IEEE Robot. Autom. Lett.* **3**(1), 387–394 (2018).
23. C. Li, J. Guo, and C. Guo, "Emerging from water: Underwater image color correction based on weakly supervised color transfer," *IEEE Signal Process. Lett.* **25**(3), 323–327 (2018).
24. J. Y. Zhu, T. Park, and P. Isola, *et al.*, "Unpaired image-to-image translation using cycle-consistent adversarial networks," arXiv preprint, (2017).
25. K. He, J. Sun, and X. Tang, "Single image haze removal using dark channel prior," *IEEE Trans. Pattern Anal. Mach. Intell.* **33**(12), 2341–2353 (2011).
26. A. Galdran, D. Pardo, A. Picón, and A. Alvarez-Gila, "Automatic Red-Channel underwater image restoration," *J. Vis. Commun. Image Rep.* **26**, 132–145 (2015).
27. N. Carlevaris-Bianco, A. Mohan, and R. M. Eustice, "Initial results in underwater single image dehazing," in *Proc. of IEEE OCEANS* (2010).
28. Y. T. Peng, X. Zhao, and P. C. Cosman, "Single underwater image enhancement using depth estimation based on blurriness," *Image Processing (ICIP), 2015 IEEE International Conference on*, IEEE (2015).
29. Y. T. Peng and P. C. Cosman, "Underwater image restoration based on image blurriness and light absorption," *IEEE Trans. Image Process.* **26**(4), 1579–1594 (2017).
30. Y. T. Peng and P. C. Cosman, "Single image restoration using scene ambient light differential," *IEEE International Conference on Image Processing, ICIP*, 1953–1957 (2016).
31. C. Li, J. Guo, S. Chen, Y. Tang, Y. Pang, and J. Wang, "Underwater image restoration based on minimum information loss principle and optical properties of underwater imaging," *IEEE International Conference on Image Processing , ICIP*, 1993–1997 (2016).
32. S. Emberton, L. Chittka, and A. Cavallaro, "Hierarchical rank-based veiling light estimation for underwater dehazing," *BMVC*, 125.1–125.12 (2015).
33. B. L. McGlamery, "A computer model for underwater camera systems," *Ocean Optics* **0208**, 221–231 (1980).
34. S. Ghosh, R. Ray, S. R. K. Vadali, and S. N. Shome, "Light-Particle interaction in underwater: a modified PSF," *Communications and Signal Processing (ICCPSP), 2014 International Conference on*, IEEE (2014).
35. T. Johnsen, H. A. Bouman, S. Sathyendranath, and E. Devred, "Regional-scale changes in diatom distribution in the Humboldt upwelling system as revealed by remote sensing: implications for fisheries," *ICES J. Mar. Sci.* **68**(4), 729–736 (2011).
36. C. L. Gallegos, D. L. Correll, and J. W. Pierce, "Modeling spectral diffuse attenuation, absorption, and scattering coefficients in a turbid estuary," *Limnol. Oceanogr.* **35**(7), 1486–1502 (1990).
37. R. Fattal, "Single image dehazing," *ACM Trans. Graphics* **27**(3), 1 (2008).
38. R. T. Tan, "Visibility in bad weather from a single image," in *Proc. of IEEE CVPR*, 1–8 (2008).
39. K. B. Gibson, D. T. Vo, and T. Q. Nguyen, "An investigation of dehazing effects on image and video coding," *IEEE Trans. Image Process.* **21**(2), 662–673 (2012).
40. J. Yu, C. Xiao, and D. Li, "Physics-based fast single image fog removal," *Proc. IEEE ICSP* **37**(2), 1048–1052 (2011).
41. C. H. Yeh, L. W. Kang, C. Y. Lin, and C. Y. Lin, "Efficient image/video dehazing through haze density analysis based on pixel-based dark channel prior," *Proc. IEEE ISIC* **238**, 14–16 (2012).
42. F. C. Cheng, C. C. Cheng, P. H. Lin, and S. C. Huang, "A hierarchical airlight estimation method for image fog removal," *Eng. Appl. Artif. Intell.* **43**, 27–34 (2015).
43. K. Wang, E. Dunn, J. Tighe, and J. M. Frahm, "Combining semantic scene priors and haze removal for single image depth estimation," in *Proc. of IEEE WACV*, 800–807 (2014).
44. R. J. Davies-Colley, "Measuring water clarity with a black disk," *Limnol. Oceanogr.* **33**(4), 616–623 (1988).
45. R. Gould, R. Arnone, and P. Martinolich, "Spectral dependence of the scattering coefficient in case 1 and case 2 waters," *Appl. Opt.* **38**(12), 2377–2383 (1999).
46. M. Yang and A. Sowmya, "An underwater color image quality evaluation metric," *IEEE Trans. Image Process.* **24**(12), 6062–6071 (2015).
47. S. Zhang, T. Wang, and J. Dong, *et al.*, "Underwater image enhancement via extended multi-scale Retinex," *Neurocomputing* **245**, 1–9 (2017).
48. Imatest, Accessed: Jan. 3, 2015. [Online]. Available: <http://www.imatest.com/>.